PERGAMON

International Journal of Heat and Mass Transfer 44 (2001) 4413–4425

International Journal of HEAT and MASS TRANSFER

www.elsevier.com/locate/ijhmt

Flow structure and local Nusselt number variations in a channel with dimples and protrusions on opposite walls

P.M. Ligrani *, G.I. Mahmood, J.L. Harrison, C.M. Clayton, D.L. Nelson

Department of Mechanical Engineering, MEB 2202, Convective Heat Transfer Laboratory, University of Utah, 50 S. Central Campus Drive, Salt Lake City, UT 84112-9208, USA

Received 10 April 2000; received in revised form 8 March 2001

Abstract

Flow structure characteristics are presented for a channel with a dimpled surface on one wall, both with and without protrusions (with the same shapes as the dimples) on the opposite wall. Channel aspect ratio is 16, ratio of channel height to dimple print diameter is 0.5, and Reynolds numbers based on channel height range from 380 to 30,000. Instantaneous flow visualization images and surveys of time-averaged flow structure show that the protrusions result in added vortical, secondary flow structures and flow mixing. As a result, local friction factors and local Nusselt numbers are augmented compared to a channel with no protrusions on the top wall. For Nusselt numbers, such augmentations are present near the downstream edges of dimple rims mostly near dimple diagonals, as well as on flat surfaces immediately downstream of dimple rims.

1. Introduction

Flow characteristics and structure are important for heat transfer augmentation in internal passages. This is because the amount of surface heat transfer augmentation is controlled by the levels and character of secondary flows, three-dimensionality, shear layer reattachment, unsteadiness, and turbulence transport induced by the devices employed on the walls of the internal passages. These include rib turbulators, arrays of pin fins, arrays of shaped roughness elements, and more recently, passage surfaces with arrays of dimples. Practical applications for these components in internal passages include macro- and micro-scale heat exchangers, electronics cooling, combustion chamber liners, passages for internal cooling of turbine airfoils in gas turbine engines, as well as many other devices. The present paper is focused on the use of dimples and protrusions on opposite walls of a channel with a rectangular cross-section.

One of the earliest investigations of flow behavior near dimpled surfaces is presented by Bearman and Harvey [1], who describe the influences of dimples placed on the surfaces of golf balls. Gromov et al. [2] describe symmetric and non-symmetric streamlines and flow patterns produced by dimple cavities with a variety of sizes, placed on a flat surface. Cells of fluid motion are described in the form of tightening spirals, helical streamlines, and horse-shoe shaped vortices. Kimura and Tsutahara [3] give the optimum concavity depth of dimples to achieve minimum drag on cylinders. At high Reynolds numbers, significantly lower drag coefficients are present with arrays of dimples compared to smooth cylinders. This optimum depth is used by Bearman and Harvey [4] for dimples placed on cylindrical surfaces in a study of surrounding cross-flows. In addition to heat transfer data, Afanasyev et al. [5] describe the flow mechanisms for heat transfer enhancements of flows over walls indented with regular arrays of spherical pits. Included are the dynamic properties and pressure losses of the boundary layer on the smooth surface between the pits.

Kesarev and Kozlov [6] describe the effects of turbulence intensity of the incident flow on the local heat flux and on the local shear stress on dimple cavity

* Corresponding author. Tel.: + 1-801-581-4240; fax: +1-801-585-9826.

E-mail address: ligrani@mech.utah.edu (P.M. Ligrani).

0017-9310/01/$ - see front matter
PII: S0017-9310(01)00101-6

Nomenclature

D	dimple print diameter
H	channel height
f	channel friction factor
f_0	baseline friction factor in channel measured with smooth top and bottom channel surfaces
k	thermal conductivity
Nu	local Nusselt number based on channel hydraulic diameter
Nu_0	baseline Nusselt number based on channel hydraulic diameter, and measured with smooth top and bottom channel surfaces
P_a	ambient pressure
P_s	time-averaged static pressure
P_t	time-averaged total pressure
Re_H	Reynolds number, $\rho\bar{U}H/\mu$
u	time-averaged streamwise component of velocity
$\bar{U}$	time-averaged bulk velocity in the channel
X	streamwise coordinate measured from upstream edge of test surface
Y	normal coordinate measured from dimple horizon surface
Z	spanwise coordinate measured from spanwise centerline of test surface

Greek symbols

ρ	density
μ	absolute viscosity
ω_x	time-averaged streamwise vorticity

surfaces. Zhak [7] describes a variety of vortex structures in different shaped rectangular cavities, determined from flow visualizations. Terekhov et al. [8] present experimental measurements of flow structure and pressure fields in a channel with a single dimple on one surface. Different magnitudes and frequencies of flow oscillations are described, along with the pressure loss dependence on dimple geometry. Gortyshov et al. [9] employs spherical dimples, called spherical intensifiers, placed at different relative positions on the two opposite surfaces of a narrow channel. Lin et al. [10] give computational simulation results which show the influences of Reynolds number on local flow structure above surfaces imprinted with staggered arrays of two different shapes of concavities. Their data for three different height channels show flow structures, flow streamlines, and temperature distributions, which provide insight into detailed flow phenomena produced by the dimples. Mahmood et al. [11] describe the mechanisms responsible for local- and spatially-averaged heat transfer augmentations on flat channel surfaces with an array of dimples on one wall. Most important are:

1. the reattachment of the shear layer which forms across the top of each dimple,
2. the vortex structures and vortical fluid shed from each individual dimple indentation which then advect over the flat surface just downstream, and
3. the periodic unsteadiness which is produced as flow is ejected and then inrushes to each dimple.

The present paper deals with the use of dimples on one channel surface, with protrusions placed on the opposite wall, as mentioned. No other study is known to exist which employs such a geometric arrangement. The effects of these protrusions on local flow structure, compared to a channel with a smooth wall in place of the one with protrusions, is the primary focus. To document this, local surveys and spatially-averaged profiles of time-averaged total pressure, static pressure, streamwise velocity, and streamwise vorticity are given. Also included are flow visualization results, obtained with protrusions on the top wall. Additional flow visualization results are given without protrusions, and with the array of protrusions positioned at several different locations with respect to the array of dimples on the opposite surface. Also presented are channel friction factors. Channel aspect ratio is 16, ratio of channel height to dimple print diameter is 0.5, and Reynolds numbers based on channel height range from 380 to 30,000. These data show overall flow structure as well as the characteristics of the vortex structures and vortical fluid shed from the protrusions and dimple indentations. These characteristics are then tied to levels of heat transfer augmentation, which are illustrated by local Nusselt number distributions measured with and without protrusions on the top surface of the channel.

2. Experimental apparatus and procedures

2.1. Channel for flow structure measurements

Schematic diagrams of the facility used for the flow structural measurements is shown in Figs. 1(a) and (b). Fig. 1(a) shows that this facility is an open-loop, suction-type flow device. At the inlet of the facility, the air passes from the laboratory into a rectangular bell mouth inlet, followed by a honeycomb, two screens, and a two-dimensional 19.5 to 1 contraction ratio nozzle. This nozzle leads to a boundary layer bleed on the top and bottom walls, followed by a rectangular cross-section, 411 mm × 25.4 mm inlet duct which is 1219 mm in length. This is equivalent to 25.4 hydraulic diameters (where hydraulic diameter is 47.8 mm). A trip is

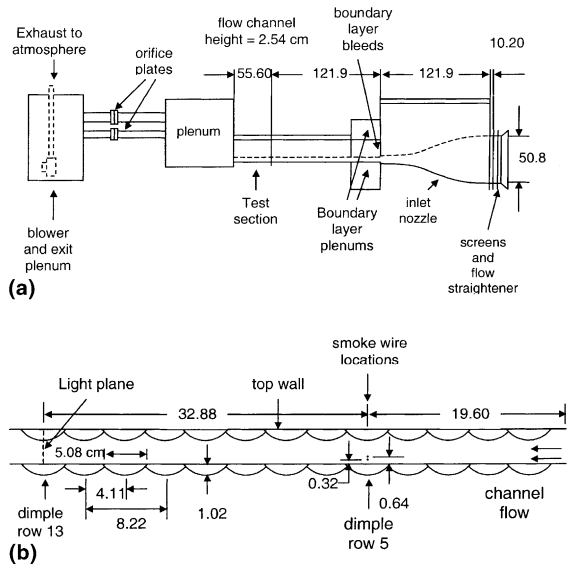

Fig. 1. Experimental facility for flow structural measurements: (a) overall facility; (b) test section detail. All dimensions given in centimeters.

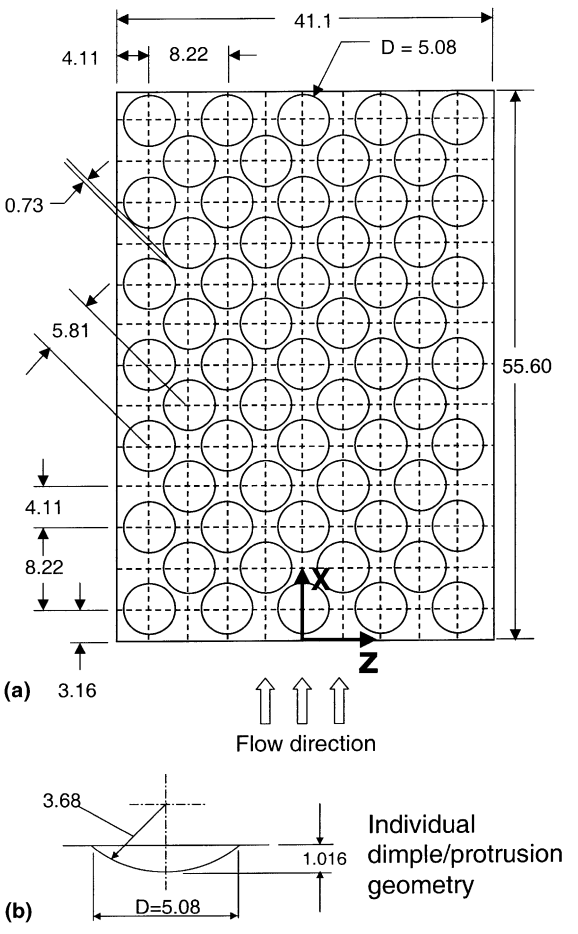

Fig. 2. Test section surfaces: (a) overall dimple and protrusion test surface geometry, including coordinate system; (b) individual dimple/protrusion geometry. All dimensions given in centimeters.

employed on the bottom surface of the inlet duct, just upstream of the test section, which follows with the same cross-section dimensions. Test section aspect ratio is then about 16, and the ratio of test section height to dimple print diameter H/D is 0.5.

A side view of the test section is shown in Fig. 1(b). From this diagram, it is apparent that the bottom surface of the test section is dimpled. For baseline measurements, this dimpled bottom surface can be replaced with a smooth bottom surface. Either a surface with protrusions (as shown in Fig. 1(b)) or a smooth surface can be employed on the top wall. The side walls are always smooth. Fig. 1(a) then shows that the test section duct exits to a 0.76 m square plenum, which is followed by two pipes, each containing an ASME standard orifice plate, for the measurement of mass flow rates when used in conjunction with a Validyne M10 digital pressure manometer. These two pipes and plates can be used independently or together, depending on the magnitudes of flow rates to be measured. Fig. 1(a) also shows that these pipes then connect to a second larger plenum. Contained inside is an ILG Industries 10P-type centrifugal blower, which is employed to induce flow through the test section. From this second plenum. the air from the facility then exits to a vent.

2.2. Test surface geometry details

Figs. 2(a) and (b) present the geometric details of the test surface, including individual dimple and protrusion geometries. Also identified in Fig. 2(a) is the test section coordinate system employed for the study. A total of 13 rows of dimples are employed in the streamwise direction, and 9 rows are employed in the spanwise direction in a staggered array on the bottom wall. The same arrangement is employed for the protrusions on the top surface (except that the protrusions protrude into the flow). Fig. 3 shows side views of the four different ways in which the protrusions are positioned with respect to the dimples. With configuration 1, or the full offset configuration, the protrusions and dimples are misaligned with each other with a streamwise distance between centers of 4.11 cm (Fig. 3(a)). With configuration 2, no offset is employed, and the protrusions and dimples are exactly aligned with each other (Fig. 3(b)). With configurations 3 and 4, the protrusions are located with a 1.27 cm forward offset, and with a 0.95 cm forward offset, respectively, between the dimple and protrusion centers (Figs. 3(c) and (d)).

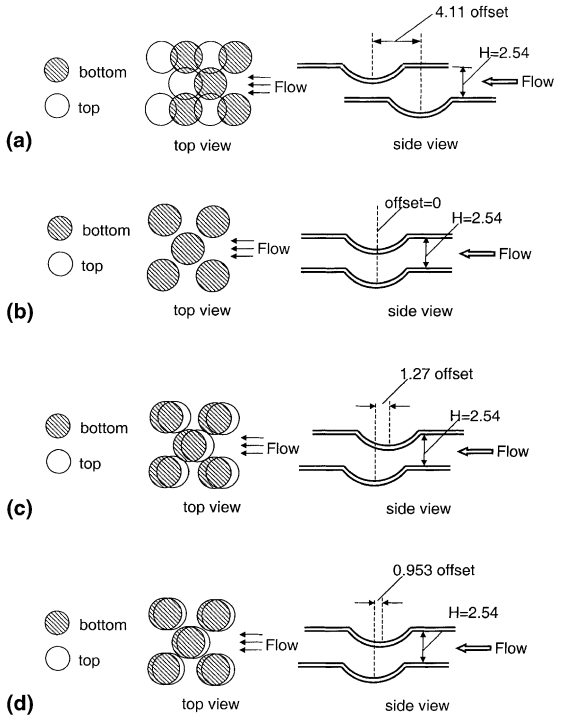

Fig. 3. Relative positions of dimples and protrusions in the test section. All dimensions given in centimeters. (a) Configuration 1, protrusions and dimples misaligned with 4.11 cm offset. (b) Configuration 2, protrusions and dimples aligned with no offset. (c) Configuration 3, protrusions and dimples misaligned with 1.27 cm offset. (d) Configuration 4, protrusions and dimples misaligned with 0.95 cm offset.

2.3. Time-averaged total pressure, static pressure, and three velocity components

A 1.27-mm outer diameter miniature five-hole pressure probe, manufactured at the University of Utah especially for these measurements, is used to obtain time-averaged surveys of total pressure, static pressure, and the three mean velocity components. These data are then used to deduce distributions of streamwise vorticity. Note that all measurements are made outside of the flow separation zones which exist within the dimples. To obtain the surveys, the probe employed is mounted on an automated two-dimensional traverse, and inserted into the test section through a slot lined with foam to prevent air leakage. The output ports of the probe are connected either to Validyne DP103-06 pressure transducers (to measure differential pressures up to 2.5 mm of water) or Celesco LCVR pressure transducers (to measure differential pressures up to 20.0 mm of water). Signals from the transducers are then processed using Celesco CD10D Carrier-Demodulators. Voltages from the Carrier-Demodulators are acquired using a Hewlett-Packard 44422A data acquisition card installed in a Hewlett-Packard 3497A data acquisition control unit. This control unit, the Superior Electric-type M092-FD310 Mitas stepping motors on the two-dimensional traverse, a Superior Electric Modulynx Mitas-type PMS085-C2AR controller, and a Superior Electric Modulynx Mitas-type PMS085-D050 motor drive are controlled by a Hewlett-Packard A4190A Series computer. Contour plots of measured quantities are generated using a polynomial interpolating technique (within DeltaGraph software) between data points. Additional details of the five-hole probe measuring procedures, including calibration details, are given by Ligrani et al. [12,13].

2.4. Flow visualization

When a smooth top wall is used, the smoke used to visualize the flow is produced from three horizontally-oriented smoke wires, located 3.2, 6.4, and 19.1 mm from the dimple surface over the 5th row of dimples at $X = 200$–210 mm (see Fig. 1(b)). When a top wall with protrusions is employed, only the two wires nearest the bottom, dimpled surface are utilized. To produce single thin planes of smoke parallel to the test surface, each wire is first coated with Barts Pneumatics super smoke fluid and then powered using a Hewlett-Packard 6433B DC power supply. As the smoke is advected downstream, the secondary flows which accompany vortex and secondary flow development cause the smoke to be rearranged in patterns which show the locations and distributions of these flow phenomena. Smoke patterns are illuminated using a thin sheet of light provided by a Colotran ellipsoidal No. 550, 1000 watt spot light, and light slits machined in two parallel metal plates. Images are recorded using a Dage-MTI CCD72 camera and control box with a Computar 12.5 mm, F1.8 lens, connected to a Panasonic AG-1960-type 4-head, multiplex video cassette recorder. Images recorded on video tape (taken individually or in sequence) are then digitized using a Sony DCR-TRV900 digital video camera recorder. The resulting images are then further processed using a Power Macintosh 7500 PC computer, and finally printed using a Panasonic PV-PD 2000 digital photo printer.

2.5. Channel for heat transfer measurements

A second channel facility, described by Mahmood et al. [11] and with the same internal test section geometry and inlet duct geometry as the first facility, is employed for heat transfer measurements. Air in the facility is circulated in a closed-loop using an ILG Industries 10P-type centrifugal blower. The blower exits into a large plenum with a Bonneville cross-flow heat exchanger located just downstream. The air then enters

a second plenum, from which the air passes into a rectangular bell mouth inlet, followed by a honeycomb, two screens, and a two-dimensional 19.5 to 1 contraction ratio nozzle. This nozzle leads to a rectangular cross-section inlet duct and test section, which then exits to a 0.60 m square plenum. This is followed by a pipe, with an ASME standard orifice plate, used to measure the air flow rate. The bottom surface of the test section is dimpled, and either a smooth surface or a surface with protrusions can be employed on the top wall. For baseline measurements, the bottom dimpled surface is replaced with an instrumented smooth surface.

All exterior surfaces of the facility (between the heat exchanger and test section) are insulated with Styrofoam ($k = 0.024$ W/m K), or 2–3 layers of 2.54 cm thick, Elastomer Products black neoprene foam insulation ($k = 0.038$ W/m K) to minimize heat losses. Calibrated copper–constantan thermocouples are located between the three layers of insulation located beneath the test section to determine conduction losses. Between the first layer and the 3.2 mm thick acrylic dimpled test surface is a custom-made Electrofilm etched-foil heater (encapsulated between two thin layers of Kapton) to provide a constant heat flux boundary condition on the test surface. The acrylic surface contains 24 copper–constantan thermocouples, and is adjacent to the air stream. Each of these thermocouples is located 0.0508 cm just below this surface to provide measurements of local surface temperatures.

2.6. Local Nusselt number measurement

Procedures for measurement of local Nusselt numbers are given by Sargent et al. [14] and Hedlund and Ligrani [15]. The associated heat transfer coefficients are based on the total area of the test surface (flat portions and dimples). Thermal conductivity in the Nusselt number is based on the average of the local wall temperature and the temperature of the air at the upstream inlet. Energy balances, performed on the heated test surface, allow determination of local magnitudes of the convective heat flux as a variac power supply is used to supply current to the foil heater. Other energy balances are used to determine the local mixed mean temperature through the test section in conjunction with measurement of the mixed mean temperature at the test section inlet, made using five calibrated copper–constantan thermocouples spread across its cross-section. All measurements are obtained when the test facility is steady-state, achieved when each of the temperatures from the 24 thermocouples (on the test surface) vary by less than 0.1°C over a 10 min period.

Spatially-resolved temperature distributions along the dimpled test surface are determined using a VideoTherm 340 Infrared Imaging Camera in conjunction with thermocouples, energy balances, digital image processing, and in situ calibration procedures [14,15]. This is accomplished as the camera views the test surface through a custom-made, zinc–selenide window located on the top wall of the test section. Reflection and radiation from surrounding laboratory sources are minimized using an opaque shield which covers the camera lens and the zinc–selenide window. During this procedure, the camera is focused, and rigidly mounted and oriented relative to the test surface in the same way as when radiation contours are recorded. Images from the infrared camera are recorded as 8-bit gray-scale images on commercial videotape using a Panasonic AG-1960 video recorder. Images are then digitized using NIH Image v1.60 software, operated on a Power Macintosh 7500 PC computer. With these data, gray-scale values at pixel locations within video taped images from the infrared imaging camera are readily converted to temperatures. Time-averaged data presented are obtained from a time-average of 40 instantaneous data sets over a time period of 40 s.

2.7. Uncertainty estimates

Uncertainty estimates are based on 95% confidence levels, and determined using procedures described by Moffat [16]. Uncertainty of temperatures measured with thermocouples is ±0.15°C . Local Nusselt number uncertainty is then about ±8.0% for a ratio of inlet stagnation temperature to surface temperature of 0.93–0.94. Corresponding local Nusselt number ratio uncertainty is about ±0.22 (for a ratio of 2.00) or ±11.3%. Reynolds number uncertainty is about ±1.7% for Re_H of 10,200. The uncertainties of total pressure (relative to atmospheric pressure), static pressure (relative to atmospheric pressure), and streamwise velocity are then about ±4.0%, ±4.0%, and ±2.5%, respectively.

3. Experimental results and discussion

3.1. Instantaneous flow structure from flow visualizations

Fig. 4 shows instantaneous flow visualization images obtained in a spanwise-normal plane at $X/H = 20.6$, and $X/D = 10.3$. Data with and without protrusions on the top wall are presented, where the protrusions are placed at different locations with respect to the dimples, as shown in Fig. 3. In each case, the magnitude of channel H/D is 0.5, and the view in Fig. 4 is obtained over the entire width of the channel, just above the center of the dimple located in the middle of the 13th row of dimples. The spanwise extent of each image approximately covers one complete period of dimple–protrusion geometry. Flow is out of the plane of the paper. Protrusions are located at the top edge of all but

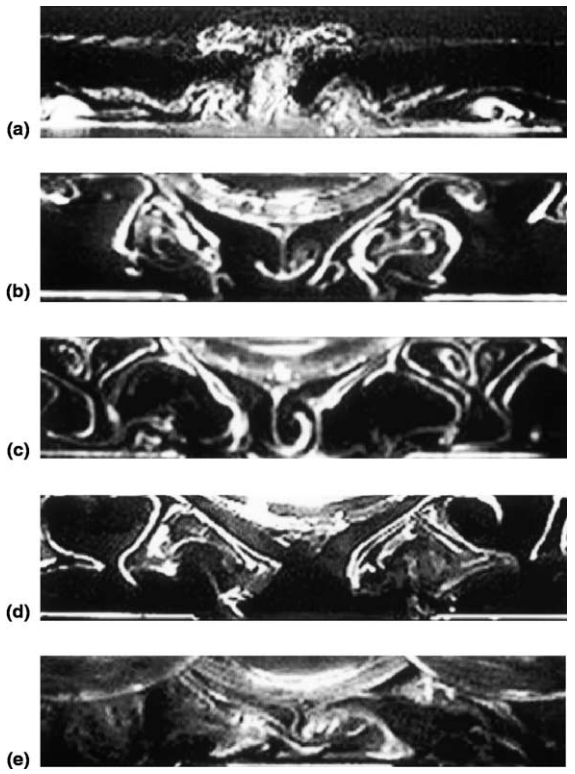

Fig. 4. Instantaneous flow visualization images obtained above the 13th row of dimples at $X/H = 20.6$, and $X/D = 10.3$: (a) $Re_H = 1170$ with smooth top wall; (b) $Re_H = 570$ with protrusions and dimples aligned with no offset (configuration 2); (c) $Re_H = 480$ with protrusions and dimples misaligned with offset of 0.95 cm (configuration 4); (d) $Re_H = 480$ with protrusions and dimples misaligned with offset of 1.27 cm (configuration 3); (e) $Re_H = 380$ with protrusions and dimples misaligned with full offset of 4.11 cm (configuration 1).

one image in Fig. 4, and dimples are located at the bottom edge all images shown in Fig. 4.

Fig. 4(a) shows a flow visualization result for $Re_H = 1170$ with smooth top wall. With this arrangement, each dimple located on the bottom surface periodically sheds a collection of vortex pairs and vortical fluid. Three such vortex pairs (identified by "mushroom-shaped" smoke patterns) are apparent in Fig. 4(a) just at or just above the horizon of (or flat surface around) the central dimple. A distinct upwash region is located between the two vortices in each pair. The most prominent of these vortex pairs and upwash regions is located centrally above each dimple center. It is often roughly symmetric with respect to a centerline/normal plane, and the associated upwash region is in the streamwise-normal plane also located approximately along the centerline of each dimple. The other two vortex pairs and associated upwash regions are located near the left and right spanwise edges of each dimple, often near diagonal dimple locations or just downstream of these locations. These vortex pairs, which form near dimple diagonals, are often in the form of collections of vortex pairs, or sometimes, short "braids" of vortical fluid [11].

All of these vortex pairs are stretched as they are advected downstream (by the streamwise bulk flow above the dimple horizon), which causes them to become smaller in cross-section, more elongated, and more distorted. As this happens, the tubes of vorticity periodically impact on the downstream rim of a dimpled edge and on the flat surface just downstream of this dimple, and then advect just above and into the dimple volumes which are located diagonal and adjacent to the originating dimple. As mentioned before, these events occur periodically. According to Mahmood et al. [11], this periodicity takes the form of a repeated cycle of events, where each cycle consists of inrush of fluid to each dimple, followed by outflow and vortex shedding. The vortices are always present temporarily at about the same locations during and after each shedding event. In addition, the vortical fluid seems to be shed simultaneously with fluid shed from other dimples in the same spanwise row, but out of phase with the packets of fluid shed from dimples in an adjacent upstream or downstream dimple row.

Figs. 4(b)–(e) show flow visualization images obtained with protrusions on the top surface of the channel, arranged in one of four different positions with respect to the dimple pattern on the bottom channel surface (see Fig. 3). Re_H ranges from 380 to 570 for these data. The cross-section of one single protrusion, or a part of one single protrusion, is evident near the top of each image in Figs. 4(b)–(e).

Compared to the flow visualization data obtained with a smooth top surface, time-varying images obtained with a protruded top wall (in Figs. 4(b)–(e)) show many important differences. First, the secondary flows (with protrusions present) cover the entire cross-section of the channel, and seem to be greater in intensity. This is indicated by greater convolutions of smoke patterns, including continuous wrapping of smoke into spiraled patterns at some locations. In contrast, when no protrusions are present (Fig. 4(a)), only three vortex pairs are present in the immediate vicinity of, and just above, each dimple. These secondary flows are present over about half of the channel height, except for the secondary flows associated with the central vortex pair and central upwash, which range all the way to the top smooth wall. With dimples *and* protrusions, different shaped smoke patterns are observed, both large and small, due to large and small secondary flows in the channel. Sometimes, these appear as mushroom-shaped patterns that again indicate the presence of vortex pairs. From three to six vortex pairs are identifiable in Figs. 4(b)–(e) (depending on protrusion pattern offset location with respect to the dimpled pattern), each with a length

scale about the same size as either the protrusion height or the dimple depth. Fig. 4(c) also shows "heart-shaped" smoke patterns present on either side of a protrusion. Within each of these is an inverted mushroom-shaped smoke pattern (indicating a vortex pair) with an upwash region (indicated by a "mushroom stem") directed downwards from the top wall.

Also readily apparent in Figs. 4(b) and (c), for no offset and 0.95 cm offset, respectively, are mushroom-shaped smoke patterns directed downwards from the apex of the centrally located protrusion. Similar structures are also believed to be present for the conditions and geometry of Figs. 4(d) and (e). However, the associated smoke patterns are not as apparent due to greater amounts of diffusion. The associated vortex pair and upwash region are due to the flow which advects around each protrusion and is then forced downwards. As it moves down towards the dimple, flow is encountered in the opposite direction (after being ejected from the dimple), and the two associated counter-rotating vortices are subsequently formed. This means that the protrusions occasionally force flow into the dimple cavities. Because of continuity, this then causes greater quantities of fluid to be ejected from each dimple (compared to a channel with a smooth top surface).

As the offset location of the protrusion pattern is changed with respect to the dimples, the character, locations, and shapes of the smoke patterns and associated secondary flows change. Patterns become more convoluted as the dimple–protrusion offset increases, and one progresses from the flow conditions of Fig. 4(b) to those of Fig. 4(e). Notice that the visualized plane is always located over the middle of the 13th row of dimples regardless of the position of the protrusions. Also apparent as Figs. 4(b)–(e) are compared is an increase in mixing as dimple–protrusion offset increases. This is evidenced by smoke patterns which are more diffuse, more spread out, and more convoluted over each visualization plane. Such behavior is especially evident in Fig. 4(e). When compared to the results in Fig. 4(a), obtained with a smooth top surface, it is evident that:

1. more mixing is present at much lower Re_H when protrusions are used, and
2. mixing and diffusion increase as the offset between protrusions and dimples increases and the channel geometry approaches the full-offset arrangement shown in Fig. 3(a).

This last point is made even more substantial when one considers that the flow conditions as one progresses from Figs. 4(b)–(e) coincide with a slight decrease of the Reynolds number based on channel height.

However, in spite of these differences, several key flow features responsible for augmentation of local heat transfer rates are present regardless of whether or not protrusions are employed on the top wall. These include the reattachment of the shear layer which forms across the top of each dimple, as well as the vortex structures and vortical fluid shed from each individual dimple indentation (especially along dimple diagonals) which then advect over the flat surface just downstream. The protrusions influence these phenomena by increasing their intensities and the spatial extents of their effects, and in doing so, cause them to produce more substantial augmentations of local heat transfer coefficients.

3.2. Time-averaged flow structure with and without protrusions on the top wall

Fig. 5 shows the locations of dimples and protrusions in relation to the data given in the four figures which follow, from a view looking upstream from the measurement location. Note that the dimples are located along the bottom wall at $Y/H = 0$, and the protrusions are located along the top wall at $Y/H = 1$. Surveys and profiles of time-averaged quantities are then presented in Figs. 6–10. These measurements are made over flow cross-sectional planes located 4.2 cm downstream of the last row of dimples, which corresponds to $X/H = 23.5$ and $X/D = 11.8$. Data are given in each figure for:

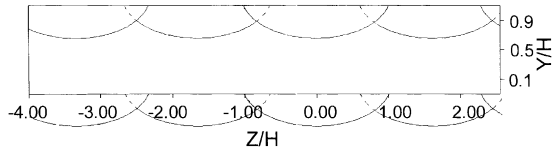

Fig. 5. Layout of spanwise-normal measurement plane for the surveys presented in Figs. 6–9 showing the locations of dimples and protrusions, looking upstream, from just downstream of the test section at $X/H = 23.5$, $X/D = 11.8$.

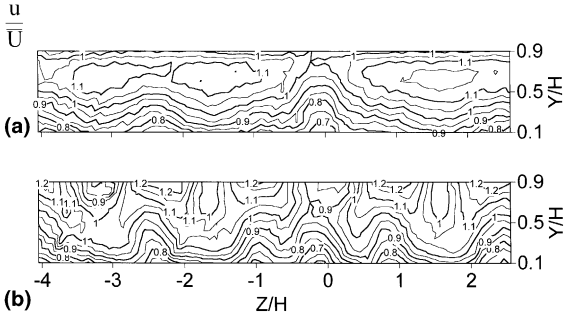

Fig. 6. Spanwise-normal plane surveys of time-averaged, normalized streamwise component of velocity u at $X/H = 23.5$, $X/D = 11.8$, or 4.2 cm downstream of the last row of dimples: (a) $Re_H = 9300$ with smooth top wall; (b) $Re_H = 8750$ with protrusions on the top wall, aligned with the dimples with no offset (configuration 2).

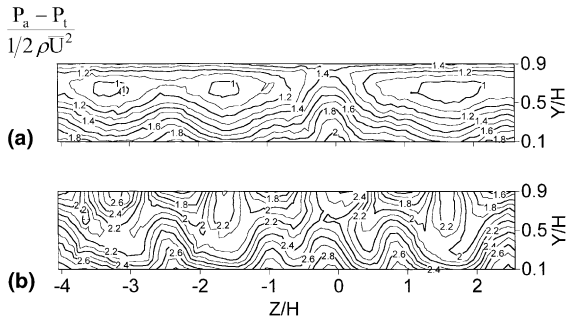

Fig. 7. Spanwise-normal plane surveys of time-averaged, normalized total pressure ($P_a - P_t$) at $X/H = 23.5$, $X/D = 11.8$, or 4.2 cm downstream of the last row of dimples: (a) $Re_H = 9300$ with smooth top wall; (b) $Re_H = 8750$ with protrusions on the top wall, aligned with the dimples with no offset (configuration 2).

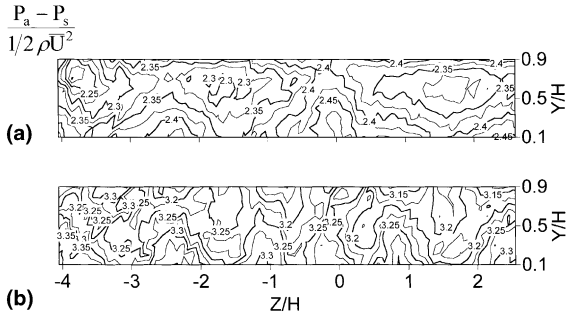

Fig. 8. Spanwise-normal plane surveys of time-averaged, normalized static pressure ($P_a - P_s$) at $X/H = 23.5$, $X/D = 11.8$, or 4.2 cm downstream of the last row of dimples. (a) $Re_H = 9300$ with smooth top wall; (b) $Re_H = 8750$ with protrusions on the top wall, aligned with the dimples with no offset (configuration 2).

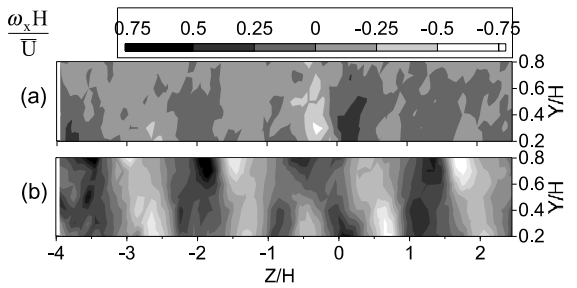

Fig. 9. Spanwise-normal plane surveys of time-averaged, normalized streamwise component of vorticity ω_x at $X/H = 23.5$, $X/D = 11.8$, or 4.2 cm downstream of the last row of dimples: (a) $Re_H = 9300$ with smooth top wall; (b) $Re_H = 8750$ with protrusions on the top wall, aligned with the dimples with no offset (configuration 2).

1. a channel with a dimpled bottom surface and a smooth top wall for $Re_H = 9300$, and

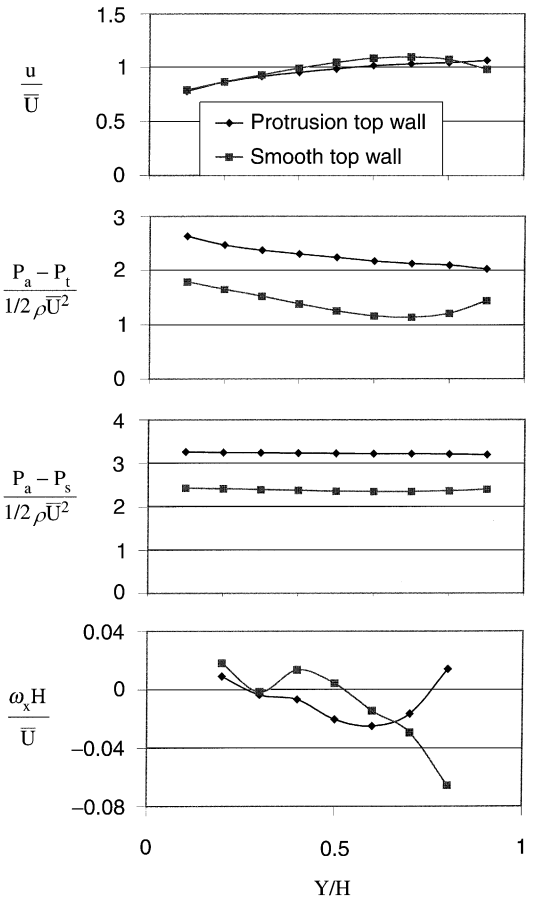

Fig. 10. Profiles of time-averaged flow properties, determined from spanwise-averages of the results presented in Figs. 6–9: (a) normalized streamwise component of velocity, $u/\overline{U}$; (b) normalized total pressure, $(P_a - P_t)/0.5\rho\overline{U}^2$; (c) normalized static pressure, $(P_a - P_s)/0.5\rho\overline{U}^2$; (d) normalized streamwise component of vorticity, $\omega_x H/\overline{U}$.

2. a channel with a dimpled bottom surface and a top wall with protrusions aligned with the dimples (i.e., oriented with no offset, configuration 2) for $Re_H = 8750$.

Given in Figs. 6–9 are normalized distributions of streamwise velocity, total pressure, static pressure, and streamwise vorticity, respectively.

The streamwise velocity data, given for a smooth top wall in Fig. 6(a), show several deficits near the dimpled surface. One of these is located just downstream of the central part of the cavity of each dimple located in the 12th and 13th dimple rows. When protrusions are present on the top wall, Fig. 6(b) shows that near-wall deficits of streamwise velocity are far more numerous and located near both the top and bottom channel surfaces. About six deficits are located in the immediate vicinity of each dimple and associated protrusion. Of the

three near the top wall, one is just downstream of the apex of the centrally located protrusion. Of the three near the bottom wall, one is just downstream of the center of the centrally located dimple, and two are located just downstream of the spanwise edges of the central dimple.

The normalized total pressure distributions in Figs. 7(a) and (b) closely mimic these streamwise velocity variations, since magnitudes and distributions of total pressure deficits are present at the same Y/H and Z/H locations. The normalized static pressure patterns in Figs. 8(a) and (b) are somewhat different from the streamwise velocity patterns in Figs. 6(a) and (b). This is because the static pressure variations across the measurement plane are influenced by bending or deflections of flow streamlines from the $+X$ direction. As a result, greater static pressure deficits are present where magnitudes of local secondary flows are larger.

The streamwise vorticity data in Figs. 9(a) and (b) are deduced from distributions of spanwise and normal velocity components. The data in Fig. 9(a), obtained in a channel with a smooth top wall and dimples on the bottom wall, show a pair of vorticity regions of opposite sign near $Z/H = 0$, which are located just downstream of the central dimple located in the 13th dimple row. Additional pairs of vorticity with opposite signs, which are somewhat less conspicuous, are located near $Z/H = +1.62$ and $Z/H = -1.62$ in Fig. 9(a), which is downstream of the central portions of dimples placed in the 12th dimple row. Each of these pairs of opposite sign vorticity are positioned on either side of deficits of total pressure and streamwise velocity shown in Figs. 6(a) and 7(a). These deficits are formed by the upwash region between the two vortices in each vortex pair.

The distributions of streamwise vorticity presented in Fig. 9(b) show six pairs of opposite sign vorticity in the vicinity of each dimple–protrusion combination. Each of these pairs is positioned around an upwash region, identified by the near-wall deficits of total pressure and streamwise velocity shown in Figs. 6(b) and 7(b). The data in Fig. 9(b) thus show good correlation with the flow visualization results in Fig. 4(b) (also for configuration 2 protrusions), considering that the two types of data are obtained at different Reynolds numbers, and at different streamwise locations (downstream of, and above, the 13th row of dimples, respectively). In some cases, regions associated with different vortex pairs, but with the same sign of vorticity, seem to be connected together in Fig. 9(b).

The profiles presented in Fig. 10 are obtained by averaging the data in Figs. 6–9 over a spanwise distance equal to the distance between the centers of two dimples located in the 13th dimple row. Presented are time-averaged profiles of the normalized streamwise component of velocity (Fig. 10(a)), normalized total pressure (Fig. 10(b)), normalized static pressure (Fig. 10(c)), and the normalized streamwise component of vorticity (Fig. 10(d)). The streamwise velocity profiles show a local maximum value near $Y/H = 0.7$ with a smooth top wall, and probably somewhere near $Y/H = 0.9$ with protrusions on the top wall. In both cases, streamwise velocities are thus somewhat lower over the portion of the channel nearest to the dimpled surface. Normalized total pressure and static pressure variations each evidence larger overall drops, relative to ambient pressure at the channel entrance, when protrusions are employed. Normalized streamwise vorticity changes dramatically when protrusions are added to the top wall of the channel. With a dimple–smooth wall arrangement, vorticity increases only as the dimpled wall is approached. With a dimple–protrusion arrangement, the spanwise-averaged streamwise vorticity increases as either wall is approached.

3.3. Friction factors and wall static pressure data with and without protrusions on the top wall

Fig. 11 shows the variation of normalized channel friction factors with Reynolds number. Data for four different channel geometries are presented: one is for a smooth top wall, and three are obtained with protrusions on the top wall (configurations 1–3). Here data are normalized using values measured in a channel with all smooth walls. According to Fig. 11, normalized f/f_0 values from a channel with protrusions and dimples on opposite walls are 2.0–2.7 times higher than values from a channel with dimples and a smooth surface on

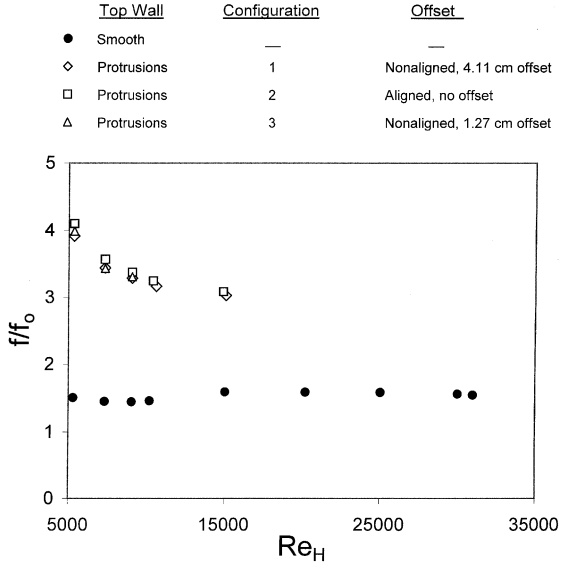

Fig. 11. Normalized channel friction factors as dependent upon Reynolds number.

opposite walls. Such data are determined from slopes of the pressure drop data (or overall changes with streamwise distance over several periods of wall static pressure variations). According to Fig. 11, overall slopes over the downstream portion of the test section (over X from 0.3 to 0.55 m) are then much higher when protrusions are employed on the top wall than when they are not.

However, regardless of whether or not protrusions are employed on the top wall, the time-averaged, surface static pressure data show distinct periodicity with streamwise development. Such results are obtained using static pressure taps along the length of the test surface, with five wall static pressure taps spaced through each dimple, and single taps located on the flat surfaces between successive dimples. Within each period of pressure variation, the highest local values are then measured within the dimples, and the lowest values come from the flat surfaces between. Variations of static pressure between the three geometries at a particular streamwise location, especially within dimples, are then due to changes of flow recirculation and shear layer reattachment from one dimple to another. When the effects of successive dimples are collected in series, overall pressure drop increases with streamwise development, regardless of the top surface configuration employed.

3.4. Local Nusselt number variations with and without protrusions on the top wall

Fig. 12 shows a schematic diagram of the dimpled test surface where local Nusselt number data are measured. This figure shows the dimpled pattern on the test surface, along with lines of constant Z/D and X/D, which correspond to the locations where local Nu/Nu_0 data are given in Figs. 13 and 14. These Nusselt number are given for a channel with a smooth top wall, and with protrusions on the top wall which are aligned with the dimples (configuration 2). Note that $Nu/Nu_0 = 1$ in these latter two figures corresponds to a channel with smooth walls on all four surfaces.

The $Z/D = -0.05$ data in Fig. 13 are located in close proximity to a line through the spanwise centerline of the central dimple in the 11th row. Notice that Nu/Nu_0 values, both with and without protrusions on the top wall, are in the vicinity of 2.0 at $7.9 < X/D < 8.2$, just upstream of the dimple. Values then decrease as X/D increases through the upstream portion of the dimple cavity, with the lowest Nu/Nu_0 magnitudes located at X/D from 8.4 to 8.7, just upstream of the center of the dimple. Here Nu/Nu_0 values measured with protrusions on the top wall are lower than values measured with a smooth top channel surface. This trend reverses itself at larger X/D from 9.0 to 9.7, where significant Nu/Nu_0 augmentations are present due to:

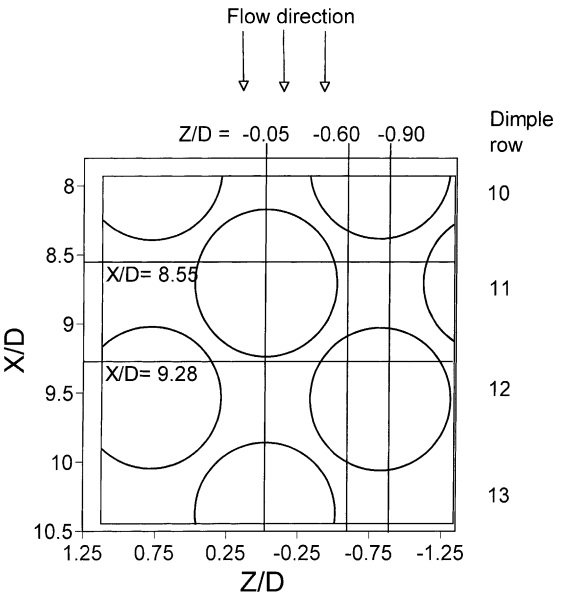

Fig. 12. Layout of the test surface showing the region for surface Nusselt number measurements, including dimple locations and lines along which data in Figs. 13 and 14 are presented.

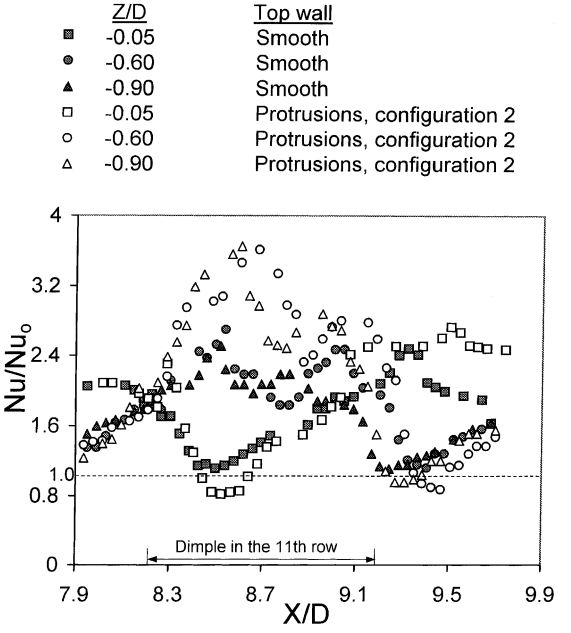

Fig. 13. Local, time-averaged Nusselt number ratios as they vary with X/D at Z/D of $-0.05, -0.60$, and -0.90 for $Re_H = 10{,}200$–$10{,}400$, and a ratio of inlet stagnation temperature to wall temperature of 0.93–0.94.

1. reattachment of the shear layer that forms across the top of each dimple, and

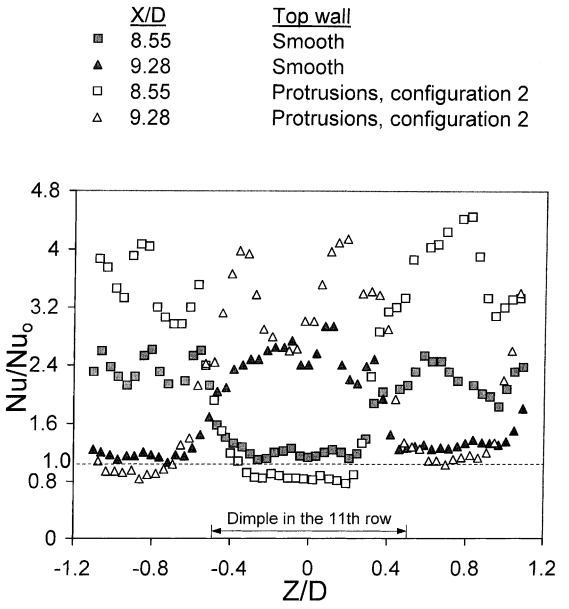

Fig. 14. Local, time-averaged Nusselt number ratios as they vary with Z/D at X/D of 8.55 and 9.28 for $Re_H = 10{,}200$–10,400, and a ratio of inlet stagnation temperature to wall temperature of 0.93–0.94.

2. increased turbulence transport resulting from vortical fluid and vortical structures shed from each dimple and then advected over the flat surface just downstream [11].

The effects of the protrusions in aiding transport by these phenomena (for $Z/D = -0.05$) are evident when the increased Nu/Nu_0 values associated with them are considered at $X/D = 9.0$–9.7, and compared to values at other X/D in Fig. 13.

According to Fig. 12, the data corresponding to Z/D of -0.60 and -0.90 in Fig. 13 are obtained on the spanwise side of the dimple in row 11. These lines pass through regions near the diagonals of an adjacent dimple in the 10th row. Such diagonal locations are clarified if each dimple is thought of as the face of a clock. Diagonals are then located along lines from the clock center to either the 7–8 o'clock region, or to the 4–5 o'clock region. With this in mind, Fig. 13 then shows that the protrusions result in considerably augmented local Nu/Nu_0 values for $X/D = 8.3 - -9.0$ and $Z/D = -0.60$ and $Z/D = -0.90$ (compared to a dimpled channel with a smooth top wall). These locations are along or near dimple diagonals near the rim of a dimple in the 10th row, as well as on flat surfaces just downstream of these diagonal positions. This provides further evidence of the effects of the protrusions in augmenting the turbulent transport capabilities of the vortices and braids of vortical fluid which form near the spanwise edges of dimples and along dimple diagonals. One factor in this process is due to continuity, which, with the obstructions provided by the dimples, results in shedding of larger volumes of higher intensity vortical fluid from each dimple.

Fig. 14 presents local Nu/Nu_0 variations with Z/D for $X/D = 8.55$ and $X/D = 9.28$. According to Fig. 12, a line through this first X/D value is located just downstream of dimples in the 10th row (at Z/D from -1.2 to -0.5, and at Z/D from $+0.5$ to $+1.2$), and through the upstream portion of dimple cavities in the 11th row (at Z/D from -0.5 to $+0.5$). Fig. 12 additionally shows that $X/D = 9.28$ is located in the upstream part of dimple cavities in the 12th row (at Z/D from -1.2 to -0.5, and at Z/D from $+0.5$ to $+1.2$), and just downstream of a dimple in the 11th row at Z/D from -0.5 to $+0.5$. Referring again to Fig. 14, local Nu/Nu_0 values are quite low, in the vicinity of 1.0, within the dimple cavities. Here values measured with protrusions on the top wall are again lower than values measured with a smooth top wall. At locations downstream of each dimple, local Nusselt numbers are augmented considerably relative to a channel with smooth walls ($Nu/Nu_0 = 1.0$). Local Nu/Nu_0 values, measured in the dimpled channel with protrusions on the top wall, are also significantly higher than values measured in a dimpled channel with a smooth top surface. Local Nu/Nu_0 additionally show two distinct peaks *downstream of each dimple* as Z/D varies. These peaks are especially evident at $X/D = 9.28$ and at Z/D from -0.5 to $+0.5$, and are due to the vortex pairs and vortical fluid shed from the spanwise edges and diagonal edges of dimples.

Note that Figs. 13 and 14 additionally show that the spatial regions with the highest local Nu/Nu_0 augmentations are slightly larger just downstream of the 10th dimple row than downstream of the 11th and 12th dimple rows. This is because no dimples are placed on the zinc–selenide window which allows the infrared camera to view the test surface. Consequently, the full effect of the protrusions on flow behavior is present near the 10th row, but not near the 11th and 12th rows. This also means that the effects of the protrusions are felt at, and immediately downstream of, their streamwise locations.

4. Summary and conclusions

Friction factors, instantaneous flow visualization images, local and spanwise-averaged distributions of time-averaged flow characteristics, and local Nusselt number data are given for a channel with rectangular cross-section and dimples on one surface, both with and without protrusions (with the same shapes as the dimples) on the opposite wall. Channel aspect ratio is 16, ratio of channel height to dimple print diameter is 0.5, Reynolds numbers based on channel height range from

380 to 30,000, and ratio of channel inlet stagnation temperature to wall temperature is 0.93–0.94.

Flow visualizations and time-averaged flow structure data show that the addition of protrusions to the top wall has a significant impact on local flow behavior. First, more extensive and stronger secondary flows are present over a much larger portion of the channel cross-section with protrusions. In addition, as many as six vortex pairs are present in the vicinity of, and downstream of, each dimple–protrusion combination (with length-scales about the size of the protrusion height or dimple depth), along with upwash regions which emanate both from the top and the bottom surface of the channel. This includes significant secondary flows downwards from the apex of each protrusion, which cause larger quantities of flow to be advected into dimple cavities than if the protrusions are not employed. These secondary flows and the flow mixing which accompanies them are also present at significantly lower Reynolds number when the protrusions are used. In contrast, the dimples produce one upwash region and vortex pair (with a length-scale on the order of the dimple depth), along with some local increases in mixing, just above, and downstream of, each dimple cavity. The protrusions thus result in additional shedding of vortical, secondary flow structures from the dimples, as well as more mixing at much lower Reynolds numbers. The protrusions aid this process as continuity causes greater quantities of fluid to be ejected from each dimple. Such behavior is also evidenced by profiles of the normalized, spanwise-averaged streamwise component of vorticity, which increases as either wall is approached with a dimple–protrusion channel arrangement.

Flow mixing also increases as the offset between protrusions and dimples increases and the protrusion pattern is more out-of-phase with the dimple surface pattern. This is evidenced by flow visualization images which become more convoluted, more diffused, and more mixed. With protrusions on the top wall, regardless of position with respect to the dimples, there also seems to be *less* large-scale periodicity and unsteadiness (over a length-scale corresponding to the size of a vortex pair) than when a smooth top wall is utilized.

The protrusions enhance the heat transfer augmentation produced by:

1. the reattachment of a separated shear layer which advects across the top of each dimple, and
2. the strong secondary fluid motions of the vortical fluid and vortex pairs which are ejected from each dimple (especially from dimple rim edges and from dimple diagonal edges) and then advect over the flat surface just downstream.

As a result, local Nusselt numbers are augmented considerably, with higher values spread over larger surface areas, compared to a channel with a smooth top wall and dimples on one opposite wall. Such changes are particularly apparent near downstream rims of dimples, near diagonal edges and spanwise edges of dimples, as well as on flat surfaces downstream of and between dimples. These are evidenced by double peaks in local Nusselt numbers just downstream of each dimple as the spanwise coordinate is varied. In contrast, in the upstream portions of the dimple cavities, local Nusselt number ratios decrease when protrusions are added to the top surface.

Friction factors are also augmented in a channel with protrusions and dimples on opposite walls. This is evidenced by values which are 2.0–2.7 times higher than values from a channel with dimples and a smooth surface on opposite walls.

Acknowledgements

Mr. M.Z. Sabbagh aided in the acquisition of a portion of the data presented.

References

[1] P.W. Bearman, J.K. Harvey, Golf ball aerodynamics, Aeronaut. Q. (1976) 112–122.
[2] P.R. Gromov, A.B. Zobnin, M.I. Rabinovich, M.M. Sushchik, Creation of solitary vortices in a flow around shallow spherical depressions, Soviet Technical Phys. Lett. 12 (11) (1986) 1323–1328.
[3] T. Kimura, M. Tsutahara, Fluid dynamic effects of grooves on circular cylinder surface, AIAA J. 29 (12) (1991) 2062–2068.
[4] P.W. Bearman, J.K. Harvey, Control of circular cylinder flow by the use of dimples, AIAA J. 31 (10) (1993) 1753–1756.
[5] V.N. Afanasyev, Y.P. Chudnovsky, A.I. Leontiev, P.S. Roganov, Turbulent flow friction and heat transfer characteristics for spherical cavities on a flat plate, Exp. Thermal Fluid Sci. 7 (1993) 1–8.
[6] V.S. Kesarev, A.P. Kozlov, Convective heat transfer in turbulized flow past a hemispherical cavity, Heat Transfer Res. 25 (2) (1994) 156–160.
[7] V.D. Zhak, The Taylor–Goertler vortices and three-dimensional flow evolution in cavity, Russ. J. Eng. Thermophys. 5 (1995) 165–176.
[8] V.I. Terekhov, S.V. Kalinina, Y.M. Mshvidobadze, Flow structure and heat transfer on a surface with a unit hole depression, Russ. J. Eng. Thermophys. 5 (1995) 11–33.
[9] Y.F. Gortyshov, I.A. Popov, R.D. Amirkhanov, K.E. Gulitsky, Studies of hydrodynamics and heat exchange in channels with various types of intensifiers, in: Proceedings of 11th International Heat Transfer Congress, vol. 6, 1998, pp. 83–88.
[10] Y.-L. Lin, T. I.-P. Shih, M.K. Chyu, Computations of flow and heat transfer in a channel with rows of hemispherical cavities, in: ASME 44th International Gas Turbine and

Aeroengine Congress and Exposition, Indianapolis, ASME Paper No. 99-GT-263, 1999.

[11] G.I. Mahmood, M.L. Hill, D.L. Nelson, P.M. Ligrani, H.-K. Moon, B. Glezer, Local heat transfer and flow structure on and above a dimpled surface in a channel, ASME Trans. – J. Turbomachinery 123 (1) (2001) 115–123.

[12] P.M. Ligrani, B.A. Singer, L.R. Baun, Spatial resolution and downwash velocity corrections for multiple-hole pressure probes in complex flows, Exp. Fluids 7 (6) (1989) 424–426.

[13] P.M. Ligrani, B.A. Singer, L.R. Baun, Miniature five-hole pressure probe for measurement of three mean velocity components in low speed flow, J. Phys. E 22 (10) (1989) 868–876.

[14] S.R. Sargent, C.R. Hedlund, P.M. Ligrani, An infrared thermography imaging system for convective heat transfer measurements in complex flows, Meas. Sci. Technol. 9 (12) (1998) 1974–1981.

[15] C.R. Hedlund, P.M. Ligrani, Local swirl chamber heat transfer and flow structure at different Reynolds numbers, ASME Trans. – J. Turbomachinery 122 (2) (2000) 375–385.

[16] R.J. Moffat, Describing the uncertainties in experimental results, Exp. Thermal Fluid Sci. 1 (1) (1988) 3–17.